X-ray Crystallographic and Solution State Nuclear Magnetic Resonance Spectroscopic Investigations of $NADP^+$ Binding to Ferredoxin NADP Reductase from *Pseudomonas aeruginosa*[†,‡]

An Wang,[§] Juan Carlos Rodríguez,[§] Huijong Han,[||] Ernst Schönbrunn,[||] and Mario Rivera*[,§]

Ralph N. Adams Institute for Bioanalytical Chemistry and Department of Chemistry, University of Kansas, Multidisciplinary Research Building, 2030 Becker Drive, Room 220 E, Lawrence, Kansas 66047, and Moffitt Cancer Center, 12902 Magnolia Drive, Tampa, Florida 33612

Received April 24, 2008; Revised Manuscript Received June 9, 2008

ABSTRACT: The ferredoxin nicotinamide adenine dinucleotide phosphate reductase from *Pseudomonas aeruginosa* (*pa*-FPR) in complex with $NADP^+$ has been characterized by X-ray crystallography and in solution by NMR spectroscopy. The structure of the complex revealed that *pa*-FPR harbors a preformed $NADP^+$ binding pocket where the cofactor binds with minimal structural perturbation of the enzyme. These findings were complemented by obtaining sequential backbone resonance assignments of this 29518 kDa enzyme, which enabled the study of the *pa*-FPR−NADP complex by monitoring chemical shift perturbations induced by addition of $NADP^+$ or the inhibitor adenine dinucleotide phosphate (ADP) to *pa*-FPR. The results are consistent with a preformed $NADP^+$ binding site and also demonstrate that the *pa*-FPR−NADP complex is largely stabilized by interactions between the protein and the 2′-P AMP portion of the cofactor. Analysis of the crystal structure also shows a vast network of interactions between the two cofactors, FAD and $NADP^+$, and the characteristic $AFVEK^{258}$ C′-terminal extension that is typical of bacterial FPRs but is absent in their plastidic ferredoxin $NADP^+$ reductase (FNR) counterparts. The conformations of $NADP^+$ and FAD in *pa*-FPR place their respective nicotinamide and isoalloxazine rings 15 Å apart and separated by residues in the C′-terminal extension. The network of interactions among $NADP^+$, FAD, and residues in the C′-terminal extension indicate that the gross conformational rearrangement that would be necessary to place the nicotinamide and isoalloxazine rings parallel and adjacent to one another for direct hydride transfer between NADPH and FAD in *pa*-FPR is highly unlikely. This conclusion is supported by observations made in the NMR spectra of *pa*-FPR and the *pa*-FPR−NADP complex, which strongly suggest that residues in the C′-terminal sequence do not undergo conformational exchange in the presence or absence of $NADP^+$. These findings are discussed in the context of a possible stepwise electron−proton−electron transfer of hydride in the oxidation of NADPH by FPR enzymes.

Ferredoxin $NADP^+$ reductases (FNRs),[1] which catalyze the reversible electron transfer between NADP(H) and their cognate ferredoxin or flavodoxin partners, are found in plastids, phototropic and heterotropic bacteria, and mitochondria (*1*). One of the best characterized enzymes is FNR from spinach leaves, a typical FNR found in plastids, which utilizes the reducing power of electromagnetic radiation to reduce $NADP^+$ and produce the NADPH needed for subsequent photosynthetic paths (*2*). In contrast, bacterial ferredoxin reductases oxidize the NADPH pool, to use this reducing potential in a large number of oxidoreductive processes. For instance, *Escherichia coli* flavodoxin reductase functions in the reduction of flavodoxin for the activation of anaerobic enzymes and in the oxidation of NADPH as a mechanism of protection against oxidative stress (*3–5*). In *Rhodobacter capsulatus* (*5*), *Azotobacter vinelandii* (*4*), and *E. coli* (*3*), the *fpr* gene encodes a ferredoxin (flavodoxin) nicotinamide adenine dinucleotide phosphate reductase (FPR) that functions in the oxidation of NADPH as a mechanism of defense against oxidative stress. A similar FPR in *Pseudomonas aeruginosa* (*pa*-FPR) has been characterized as a 258-residue NADPH-dependent enzyme that uses FAD as a cofactor (*6*). Although it is possible that *pa*-FPR also functions in mitigating oxidative stress (*4*), it has been shown that under iron starvation conditions it functions by shuttling electrons from NADPH to a heme

[†] This work was supported by Grant GM-50503 from the National Institutes of Health (M.R.).

[‡] Coordinates for the structure of the *pa*-FPR−NADP complex have been deposited in the Protein Data Bank as entry 3CRZ. Backbone resonance assignments for *pa*-FPR have been deposited in the BMRB as entry 15788.

* To whom correspondence should be addressed: Ralph N. Adams Institute for Bioanalytical Chemistry and Department of Chemistry, University of Kansas, Multidisciplinary Research Building, 2030 Becker Dr., Room 220E, Lawrence, KS 66047. Phone: (785) 864-4936. Fax: (785) 864-5396. E-mail: mrivera@ku.edu.

[§] University of Kansas.

[||] Moffitt Cancer Center.

[1] Abbreviations: FNR, ferredoxin $NADP^+$ reductase; *pa*-FPR, *P. aeruginosa* ferredoxin nicotinamide adenine dinucleotide phosphate reductase; *Av*-FPR, *A. vinelandii* ferredoxin reductase; FAD, flavin adenine dinucleotide; NAD(P)H, nicotinamide adenine dinucleotide (phosphate); IPTG, isopropyl 1-thiol-D-galactopyranoside; DTT, dithiothreitol.

10.1021/bi8007356 CCC: $40.75
Published on Web 07/08/2008

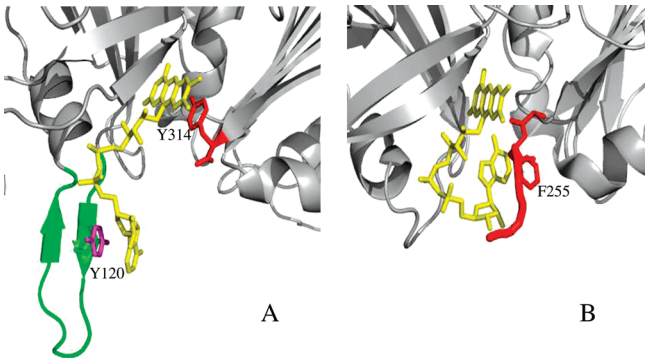

FIGURE 1: (A) Fold of plastidic FNRs that exhibits a conserved sheet−loop−sheet motif (green) that contributes to stabilization of the extended FAD (yellow) conformation characteristic of these enzymes. (B) Fold of bacterial FPRs devoid of the sheet−loop−sheet motif and exhibiting a characteristically bent FAD conformation and a C′-terminal extension (red).

oxygenase, thus supporting the process of releasing iron from exogenously acquired heme for subsequent metabolic use (*6*).

The crystal structure of *pa*-FPR (*6*) revealed a fold very similar to that characteristic of the FNR superfamily and is almost identical to the structure of FPR from *A. vinelandii* (*Av*-FPR) (*7*), *R. capsulatus* (*8*), and *E. coli* flavodoxin reductase (*9*). Comparative analysis of the X-ray crystal structures of ferredoxin reductases uncovered some interesting differences in the context of a similar fold. These differences led to the classification of these enzymes as reductases of the plastidic class, i.e., enzymes from chloroplasts and cyanobacteria, and enzymes of the bacterial class, which are further subdivided into proteobacteria subclass I enzymes (*A. vinelandii*, *R. capsulatus*, and *P. aeruginosa*) and proteobacteria subclass II reductases (*E. coli* flavodoxin reductase) (*10*). The structures showed that plastidic FNRs and bacterial FPRs differ in the conformation and chemical environment of the FAD cofactor. In the plastidic enzymes, the FAD is bound in an extended conformation, which is stabilized by specific interactions with residues in a sheet−loop−sheet motif (green in Figure 1A). These encompass π-stacking of the adenine ring with the conserved aromatic side chain of Tyr120 and hydrogen bonding interactions involving the 2′-P AMP moiety. In comparison, bacterial FPRs lack the sheet−loop−sheet motif that stabilizes the extended FAD conformation; thus, the cofactor adopts a folded conformation, where the adenine ring π-stacks with the conserved aromatic side chain of residue 255 (Figure 1B). The FMN portion of FAD in plastidic and bacterial reductases exhibits very similar conformations and chemical environments. Additional important differences occur in the carboxyl-terminal domains, which are typically thought to be involved in NADP(H) binding. Whereas in plastidic FNRs the carboxyl-terminal Tyr (Y314 in spinach FNR, Y308 in pea FNR, and Y303 in *Anabaena* FNR) π-stacks against the isoalloxazine ring of FAD (*11, 12*) (see Figure 1A), in subclass I bacterial FPRs this residue is replaced with Ala254, which is followed by a FVEK^{258} terminal sequence (Figure 1B). In the structures of *pa*-FPR and *Av*-FPR, the carbonyl oxygen of Ala254 packs against the isoalloxazine ring, replacing the conserved π-stacking interaction between the carboxyl-terminal Tyr ring and the isoalloxazine ring seen in plastidic FNRs. In subclass II bacterial enzymes, a conserved terminal Trp is found immediately after the position occupied by the terminal Tyr in plastidic enzymes, thus extending the carboxyl-terminal domain by only one residue. In these enzymes, FAD also adopts a folded conformation.

The binding of NADP+ to FNRs has been the subject of intense investigations. Cocrystallization of *Anabaena* FNR (*13*) with NADP+ revealed a complex in which the 2′-P AMP portion of the cofactor is stabilized in a manner similar that observed in the NADP+ complex obtained by soaking crystals of the *Anabaena* enzyme in a NADP+ solution (*14*). The conformation of the nicotinamide portion of the cofactor, however, is clearly distinct in the two structures. In the structure of *Anabaena* FNR obtained from crystals soaked in NADP+ solutions, the nicotinamide ring extends toward the surface of the protein and away from the isoalloxazine ring, whereas in the structure obtained from cocrystallization with NADP+, the side chain of the carboxyl-terminal Tyr (Y303) is stacked between the nicotinamide and isoalloxazine rings. The latter structure resembles more the "productive" interactions seen in other flavoenzyme families that are structurally and functionally different from FNRs (i.e., glutathione reductase) where the nicotinamide and isoalloxazine rings stack parallel and adjacent to one another (*15, 16*). Nevertheless, the side chain of Tyr303 is not displaced to allow direct overlap of the cofactor rings, as one would expect in a productive complex that facilitates direct hydride transfer. A productive complex was observed only in Y308 mutants (the C′-terminal residue) of pea FNR, where the NADP+ nicotinamide ring is nearly parallel and adjacent to the FAD isoalloxazine ring (*17*).

These observations have led to the conclusion that binding of NADP+ to FNRs is a two-step process (*17*). In the first step, the 2′-P AMP moiety binds tightly and anchors the cofactor, whereas the niconinamide portion is disordered. In the second step, the enzyme−cofactor complex is expected to sample a set of productive conformations in which the side chain of the C′-terminal Tyr is displaced, thus allowing overlap of the nicotinamide and isoalloxazine rings to facilitate hydride transfer. In the context of this mechanism, it is significant that in the structures of FPRs from *A. vinelandii*, *R. capsulatus*, and *P. aeruginosa* the terminal Tyr is replaced with Ala254, which is followed by a C′-terminal extension (AFVEK^{258}). This extension of the sequence, in principle, can be expected to slow the rate of conformational rearrangements needed to access the productive conformation of cofactors thought to facilitate direct hydride transfer, assuming that the binding of NADP+ is similar in FNRs and FPRs. Nevertheless, nothing is known about the structural properties of the NADP(H) complex of FPRs, and the functional role, if any, played by the C′-terminal extension characteristic of these enzymes has so far been elusive. In this report, we present the X-ray crystal structure of the *pa*-FPR−NADP complex, which shows an extensive network of interactions between FAD, NADP+, and the C′-terminal extension. Complementary observations made with the aid of NMR spectroscopy in solution support the notion inferred from analysis of the network of interactions in the crystal structure that the C′-terminal tail is not dynamically active, even upon NADP+ binding. These findings, which suggest that the C′-terminal extension will likely not be readily displaced to allow productive packing of the isoalloxazine

and nicotinamide rings for direct hydride transfer, are discussed in the context of a possible multistep hydride transfer at work in the oxidation of NADPH by FPR enzymes.

EXPERIMENTAL PROCEDURES

Expression of Labeled pa-FPR for NMR Studies. pa-FPR was expressed and purified following previously reported protocols (*6*). For the expression of ^{15}N-labeled *pa*-FPR, 1.0 L cultures were incubated at 37 °C in medium containing nonlabeled nutrients. Upon reaching midlog phase, the cells were centrifuged and transferred to the same volume of fresh minimum medium containing labeled $^{15}NH_4Cl$ (1.0 g/L) and cultured to an optical density at 600 nm (OD_{600}) of approximately 0.7. The culture was then transferred to a shaker incubator pre-equilibrated at 10 °C where the cells were cultured for 30 min to allow thermal equilibrium to be reached. Protein expression was then induced by addition of IPTG (final concentration of 0.3 mM), followed by culturing at 10 °C for approximately 14 h before harvesting by centrifugation. Uniformly ^{13}C- and ^{15}N-labeled *pa*-FPR, [U-^{13}C,^{15}N]-*pa*-FPR, was expressed in a similar manner, except that cells centrifuged after reaching midlog phase were resuspended in minimal medium containing $^{15}NH_4Cl$ (1.0 g/L) and [$^{13}C_6$]-D-glucose (2.0 g/L). Prior to expression, the ArcticExpress RIL cells harboring the recombinant plasmid containing the *pa-fpr* gene were adapted to grow in D_2O using a protocol similar to that reported for the expression of deuterated proteins in *Pichia pastoris* (*18*). In short, cells were plated on an LB-ampicillin plate and grown at 37 °C for 16 h. An isolated colony from this plate was transferred to 10 mL of LB-ampicillin medium containing 25% D_2O (v/v), and the cells were grown at 37 °C overnight. The resultant cell suspension was used to plate LB-agar containing 25% D_2O, and the cells were grown at 37 °C for 16 h. An isolated colony from this plate was transferred to 10 mL of LB-Amp medium [50% (v/v) D_2O] to start a new cycle of adaptation. Subsequent cycles were carried out similarly and included adaptation at 75 and 95% D_2O. Cells grown in 95% D_2O were used to make a glycerol stab culture stock. A single colony of cells grown in an LB-amp plate made with 95% D_2O was transferred to 10 mL of LB-Amp (99.9% D_2O) and cultured at 37 °C and 220 rpm overnight. This culture was used to inoculate 100 mL (99.9% D_2O) of M9 medium containing $^{15}NH_4Cl$ (1.0 g/L) and [$^{13}C_6$]-D-glucose (2.0 g/L), and the cells were grown at 37 °C to an OD_{600} of ~0.7. Fifty milliliters from this culture was used to inoculate 1.0 L of M9 medium (99.9% D_2O) containing $^{15}NH_4Cl$ (1.0 g/L) and [$^{13}C_6$]-D-glucose (2.0 g/L), and the cells were grown to an OD_{600} of ~0.7 at 37 °C. The culture was then equilibrated at 10 °C, followed by induction of protein expression by the addition of IPTG (final concentration of 0.2 mM) and culturing at 10 °C for 30 h. Cell harvesting, cell lysis, and enzyme purification were carried out as described previously (*6*). Amide and side chain deuterons were exchanged for hydrogen as follows. Pure protein was dissolved in 50 mM sodium phosphate buffer (pH 7.0) containing 8 M urea, 100 mM NaCl, and 0.1 mM FAD to a final concentration of ~8 μM and incubated at 37 °C for 3 h. This solution was dialyzed extensively against 50 mM sodium phosphate (pH 7.0) containing 100 mM NaCl, 10% (v/v) glycerol, 0.1 mM EDTA, and 5 mM DTT at 4 °C. The resultant solution was concentrated by ultrafiltration (Centricon-10, molecular mass cutoff of 10 kDa) to 1.0 mL, loaded onto a Sephadex G-50 column (100 cm × 1.6 cm) to remove free FAD, and eluted with 50 mM sodium phosphate buffer (pH 7.0).

Selective amino acid labeling of *pa*-FPR was carried out following a protocol reported previously (*19*) with some modifications (*20*). The minimal medium used to obtain uniformly labeled protein was supplemented with the following amino acids: 0.5 g/L L-Ala, 0.4 g/L L-Arg, 0.4 g/L L-Asp, 0.4 g/L L-Asn, 0.05 g/L L-Cys, 0.4 g/L L-Gln, 0.65 g/L L-Glu, 0.55 g/L Gly, 0.1 g/L L-His, 0.23 g/L L-Ile, 0.23 g/L L-Leu, 0.42 g/L L-Lys hydrochloride, 0.25 g/L L-Met, 0.13 g/L L-Phe, 0.1 g/L L-Pro, 2.10 g/L L-Ser, 0.23 g/L L-Thr, 0.17 g/L L-Tyr, 0.23 g/L L-Val, and 0.05 g/L L-Trp. All amino acids except L-Trp and the ^{15}N-enriched amino acid were added in solid form to the medium prior to autoclaving. [^{15}N]Trp was filter sterilized and added prior to inoculation. For the preparation of [[^{15}N]Leu]-*pa*-FPR, 10 mL of LB medium was inoculated with a single colony and grown overnight at 37 °C. The overnight culture was used to inoculate 1.0 L of M9 medium supplemented as described above, but not containing L-Leu. The cells were grown at 37 °C to an OD_{600} of ~0.7, equilibrated at 10 °C, and supplemented with [^{15}N]-L-Leu prior to induction of protein expression by the addition of IPTG (final concentration of 0.2 mM) and cultured for 12−15 h. The same process was used to prepare *pa*-FPR labeled selectively with [^{15}N]Val, [^{15}N]Glu, [^{15}N]Phe, and [^{15}N]Asp. A slight modification was needed to prepare enzyme labeled with [^{15}N]Tyr, [^{15}N]Phe, and [^{15}N]Thr. In the preparation of [[^{15}N]Tyr]-*pa*-FPR and [[^{15}N]Phe]-*pa*-FPR, 0.25 g of glyphosate (*N*-phosphonomethyl-glycine) was added together with the ^{15}N-labeled amino acid. In the preparation of [[^{15}N]Thr]-*pa*-FPR, additional 0.23 g/L L-Ile and 0.115 g/L L-Val were added together with the [^{15}N]Thr to minimize isotope scrambling to Ile or Val. In the preparation of [[^{15}N]Gly]-*pa*-FPR, the relatively minor scrambling from [^{15}N]Gly to [^{15}N]Ser was intentionally preserved because it was useful in the identification of cross-peaks originating from Ser residues in *pa*-FPR. Cell harvesting, cell lysis, and enzyme purification were carried out as described previously (*6*).

NMR Sample Preparation. Protein concentrations were determined by measuring the absorption of *pa*-FPR solutions at 450 nm (ε_{450} = 11.5 mM^{-1} cm^{-1}) (*6*). NMR samples typically contained 0.1−1.2 mM *pa*-FPR and 5−10% D_2O in 50 mM sodium phosphate buffer (pH 7.0). The details of the experimental conditions used for specific NMR experiments are given in the appropriate figure captions.

NMR Spectroscopy and Backbone Resonance Assignments. NMR experiments were carried out in a Bruker Avance 800 spectrometer equipped with a 5 mm TXI ^{1}H-^{13}C/^{15}N/D_{xyz} gradient probe. Two- and three-dimensional NMR experiments [^{1}H−^{15}N HSQC, ^{1}H−^{15}N TROSY-HSQC, HNCA, HN(CO)CA, TROSY-HNCACB, TROSY-HN(CO)CACB, TROSY-HN(CA)CO, and TROSY-HNCO] for NMR assignment were carried out at 25 °C. For amino acid selective ^{15}N-labeled *pa*-FPR, [[^{15}N]Gly]-*pa*-FPR, [[^{15}N]Leu]-*pa*-FPR, [[^{15}N]Val]-*pa*-FPR, [[^{15}N]Glu]-*pa*-FPR, [[^{15}N]Phe]-*pa*-FPR, [[^{15}N]Asp]-*pa*-FPR, [[^{15}N]Tyr]-*pa*-FPR, and [[^{15}N]Thr]-*pa*-FPR were used to acquire ^{1}H−^{15}N HSQC spectra. Two- and

three-dimensional NMR spectra were processed using NMRPipe and analyzed with Sparky. ^{1}H chemical shifts were referenced to the proton resonance of DSS at 0 ppm, while ^{15}N and ^{13}C shifts were referenced indirectly using ratios of 0.101329118 and 0.251449530, respectively (*21*).

Chemical Shift Perturbation Experiments. $^{1}H-^{15}N$ HSQC spectra were recorded at 25 °C using Varian Unity Inova 600 MHz and Bruker Avance 800 MHz spectrometers. [^{15}N]-*pa*-FPR (500 μL, 0.25 mM) in 50 mM sodium phosphate (pH 7.0, 10% D_2O) contained in a 5 mm diameter NMR tube was titrated with a stock solution of $NADP^+$ (39 mM) dissolved in the same buffer. Titrations were carried out by addition of 0.05, 0.10, 0.20, 0.30, 0.40, 0.50, 0.75, 1.0, 1.5, 2.0, 3.5, 5.0, 7.5, 10, 15, 20, and 25 equiv of $NADP^+$ relative to *pa*-FPR. The pH of the solution after the addition of each aliquot of $NADP^+$ was adjusted to 7.0 prior to recording the corresponding $^{1}H-^{15}N$ HSQC spectrum. The spectra were acquired at 25 °C using a Varian Unity Inova 600 MHz spectrometer. The data were processed using NMRpipe and analyzed using Sparky. Similar experiments were carried out with adenosine 2′,5′-diphosphate (ADP), a competitive inhibitor of ferredoxin reductase enzymes.

X-ray Crystallography. X-ray-quality single crystals of *pa*-FPR in complex with $NADP^+$ were grown using the hanging drop vapor diffusion method by mixing 2 μL of *pa*-FPR (20 mg/mL) dissolved in 20 mM Tris (pH 7.6) containing 10 mM $NADP^+$ with 2 μL of a solution consisting of 200 mM ammonium acetate, 100 mM sodium citrate tribasic dihydrate, and 25% PEG-4000 (pH 5.6). Diffraction data were recorded at −180 °C using the rotation method on a single flash-frozen crystal [detector, R-axis IV^{++} image plate; X-rays, Cu Kα, focused by mirror optics; generator, Rigaku model RU300 (MSC, The Woodlands, TX)]. The cryoprotectant was 20% ethylene glycol. X-ray data were reduced with XDS (*22*); CNS (*23*) was employed for phasing and refinement, and model building was performed with O (*24*). The structure was determined by molecular replacement using the coordinates of ferredoxin oxidoreductase from *pa*-FPR (PDB entry 2QDX) as a search model, stripped of solvent molecules and ligands. Refinement was performed using data to the highest resolution with no σ cutoff applied. Several rounds of minimization simulated annealing (starting temperature of 2500 K) and restrained individual *B*-factor refinement were carried out. Data collection and refinement statistics are summarized in Table 1.

Table 1: Summary of Data Collection and Structure Refinement[a]

data set	FPR(FAD)−$NADP^+$ complex
space group	$P2_12_12$
unit cell dimensions	$a = 67.14$ Å, $b = 73.49$ Å, $c = 51.54$ Å, $\alpha = \beta = \gamma = 90°$
no. of protein atoms	2037 (average *B*-factor = 22.5 Å^2)
no. of ligands	FAD and $NADP^+$ (101 atoms) (average FAD *B*-factor = 19.4 Å^2) (average $NADP^+$ *B*-factor = 24.4 Å^2)
no. of solvent molecules	288 (average *B*-factor = 33.1 Å^2)
rmsd[b] for bonds (Å)	0.01
rmsd[b] for angles (deg)	1.7
resolution range (Å)	20−1.90 (1.95−1.90)
no. of unique reflections	20561 (2895)
completeness (%)	99.7 (99.4)
$I/\sigma I$	28.45 (8.44)
R_{merge} (%)	3.8 (15.7)
R_{cryst}[c] (%)	18.1
R_{free}[d] (%)	21.8

[a] Values in parentheses refer to the highest-resolution shell. [b] Root-mean-square deviation from ideal values. [c] $R_{cryst} = 100 \times \sum|F_{obs} - F_{model}|/\sum F_{obs}$, where F_{obs} and F_{model} are observed and calculated structure factor amplitudes, respectively. [d] R_{free} is the R_{cryst} calculated for randomly chosen unique reflections, which were excluded from the refinement (1234 for FPR liganded with FAD).

RESULTS AND DISCUSSION

Precedents guiding current views of hydride transfer between flavin and nicotinamide are grounded in observations made with the structure of glutathione reductase, a flavoenzyme that is functionally and structurally different from FNR (*15, 16*). The structure of glutathione reductase shows the nicotinamide ring parallel and adjacent to the isoalloxazine ring; this relative orientation, which likely facilitates direct hydride ion transfer, is viewed as a productive complex. In the structures of plastidic FNRs, however, the side chain of the C′-terminal Tyr lies parallel to the flavin isoalloxazine ring, thus occupying the place that would be taken by the nicotinamide ring in a productive complex. Work aimed at explaining these structural observations led to the hypothesis that $NADP^+$ binding to plastidic FNRs is a two-step process, with the first step involving strong interactions between the 2′-adenosyl phosphate moiety and FNR, whereas the nicotinamide portion undergoes less specific interactions with the enzyme. In the second step, the side chain of the terminal Tyr moves and allows the nicotinamide ring to stack parallel to the isoalloxazine ring, thus forming a transient but productive complex conducive to direct hydride transfer (*17*).

In comparison, prior to this report, virtually nothing was known regarding the binding of $NADP^+$ to bacterial FPRs. Amino acid sequence alignments and the structures of *Av*- and *pa*-FPRs had demonstrated that the position occupied by the terminal Tyr in FNRs is occupied by Ala in the bacterial enzymes (A254 in *pa*-FPR), where the carbonyl oxygen of this residue stacks against the isoalloxazine ring of FAD (*6, 7*). In addition, FPR enzymes possess a characteristic C′-terminal extension following A254 ($AFVEK^{258}$). The effect of $NADP^+$ binding on the interaction between A254 and FAD and on the conformation of the C′-terminal extension, however, was difficult to predict. The structure of the *pa*-FPR−NADP complex reported herein provides a first view of the interactions between $NADP^+$ and *pa*-FPR. As we will show below, analysis of the structure shows a vast network of stabilizing interactions among FAD, $NADP^+$, and the C′-terminal extension, which suggests that the gross conformational rearrangements that would be needed for placing the nicotinamide and isoalloxazine rings parallel and adjacent are not likely to occur. These observations are discussed in the context of a putative mechanism where the oxidation of NADPH by FPRs may occur via stepwise rather than direct hydride transfer.

The Crystal Structure of the pa-FPR−NADP Complex Shows a Network of Interactions Encompassing FAD, $NADP^+$, and the C′-Terminal Extension. The recently reported crystal structure of *pa*-FPR (*6*) showed that the enzyme folds into a two-domain structure, typical of the ferredoxin $NADP^+$ reductase superfamily. The FAD cofactor binds in the N-terminal domain (residues 1−87), comprised of an antiparallel β-barrel (β1−β6) capped by helix α1. The stabilizing interactions between FAD and *pa*-FPR have been

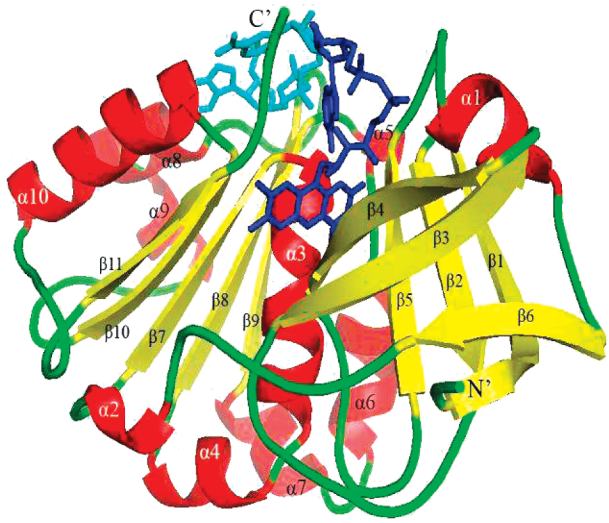

FIGURE 2: View of the structure of *pa*-FRP bound to $NADP^+$. FAD is colored blue and $NADP^+$ cyan; α-helices are colored red, *β*-sheets yellow, and loops green.

described in detail previously (*6*); these interactions remain largely unchanged in the structure of the *pa*-FPR−NADP complex, which shows that $NADP^+$ binds in the C′-terminal domain of the *β*-sheet, comprised of *β*7, *β*10, the loop connecting *β*7 to α3, the N-terminal residues of α3, and carboxyl-terminal residues $AFVEK^{258}$ (Figure 2). There are several stabilizing interactions between the polypeptide and the cofactor (Figure 3). Starting at the adenine end of the $NADP^+$ molecule, the nitrogen of the NH_2 group in this ring is within hydrogen bonding distance of the hydroxyl oxygen in Ser223 and the carboxylate group of Glu227. The 2′-phosphate (2′-P) is anchored to the enzyme via H-bonds and salt bridges to the hydroxyl oxygen of Thr181, the guanidinium NH and NH_2^+ groups in the side chain of Arg182, and the guanidinium NH group of Arg190. A salt bridge between the negatively charged oxygen in the pyrophosphate P1 group of $NADP^+$ and the guanidinium NH_2^+ group of Arg145 and a hydrogen bond between the NH group of the same side chain and the neutral oxygen in P1 stabilize this portion of the cofactor. The 1′- and 2′-hydroxyl groups in the nicotinamide ribose ring of $NADP^+$ are engaged in hydrogen bonding interactions with the adenine N3 atom and with the ribose 2-hydroxyl groups of FAD, respectively. It is important to point out that despite the proximity suggested by these interactions, the isoalloxazine and nicotinamide rings of FAD and $NADP^+$ are separated by the C′-terminal residues. This network is expanded by *π*-stacking interactions between the adenine ring in FAD and the aromatic side chain of Phe255; the latter is also T-stacked against the nicotinamide ring of $NADP^+$. The nicotinamide amide NH and carbonyl groups are within hydrogen bonding distance of the carboxylate group in Glu257 and the backbone NH group of Ser 223, respectively. The carboxylate group of Glu257 expands the network by hydrogen bonding with the 1-hydroxyl group in the AMP portion of FAD. Lys258 complements the network with electrostatic and hydrogen bonding interactions with FAD that involve the side chain NH_3^+ group with the 2-pyrophosphate group and the terminal carboxylate with the 2′-ribityl hydroxyl, respectively.

Three important observations emerge from this analysis. (1) Residues in the $AFVEK^{258}$ extension form an integral part of a complex network of interactions that associate the FAD and $NADP^+$ cofactors with the enzyme. (2) The C′-terminal extension would have to undergo extensive conformational rearrangements to permit the formation of a productive complex with the nicotinamide and isoalloxazine rings stacked parallel and adjacent to one another. (3) Parallel stacking of these rings would also require large conformational changes in FAD, which would have to change from its folded conformation to perhaps the extended conformation characteristic of plastidic FNRs. This is unlikely because the folded conformation of FAD is stabilized by the network of interactions with $NADP^+$ and the C′-terminal extension and because the absence of a sheet−loop−sheet motif in FPRs (see Figure 1) renders the enzyme incapable of stabilizing FAD in its extended conformation.

Consequently, in the context of current models for $NADP^+$ binding to plastidic FNR enzymes, it seems unlikely that binding of the cofactor to *pa*-FPR would trigger the gross conformational rearrangement needed to allow parallel and adjacent placement of the nicotinamide and isoalloxazine rings in the *pa*-FPR−NADP complex. This in turn suggests that formation of a productive complex, in the sense of $NADP^+$ binding to plastidic FNR, is not likely to occur with a frequency (microseconds to milliseconds) conducive to catalytical competence.

The Structure of pa-FPR Harbors a Preformed $NADP^+$ Binding Pocket. The binding of $NADP^+$ brings about relatively minor structural changes to *pa*-FPR, which can be seen in the per-residue plot of ΔC_α (Figure 4A), obtained by aligning the structures of *pa*-FPR and the *pa*-FPR−NADP complex. The largest differences in C_α position, taken as ΔC_α being >1.5 times the average rmsd (0.47 Å) obtained from the alignment, are localized in the N-terminal of helix α10 (residues 221−225), the middle of the loop connecting α10 to *β*11 (residues 242−244), and the carboxyl-terminal Lys258. Among the affected amino acids, residues 221−225 and 258 are located in the proximity of the bound $NADP^+$, whereas residues 242−244 are distant; the differences in C_α position seen for the latter are likely a consequence of the higher-than-average *B*-factors exhibited by these residues. Panels B and C of Figure 4 illustrate a portion of the surface of *pa*-FPR and the *pa*-FPR−NADP complex, respectively. The side-by-side comparison reveals that the surface of *pa*-FPR has a preformed cavity where the $NADP^+$ cofactor binds to form the *pa*-FPR−NADP complex with minimal perturbation of the *pa*-FPR structure.

It is well-known that $NADP^+$-dependent enzymes cannot substitute this cofactor for NAD^+, a fact that is also evident in the negligible catalytic activity observed with *pa*-FPR when NADPH is replaced with NADH (*6*). Site-directed mutagenesis studies indicated that stabilization of the 2′-P in $NADP^+$ contributes significantly to the mechanism whereby NADP(H)-dependent FNR enzymes discriminate against NAD(H) (*25, 26*). In this context, it is interesting that in the crystal structure of *pa*-FPR a sulfate anion (from the crystallization solution) is nearly isostructural with the 2′-P group of $NADP^+$ in the crystal structure of the *pa*-FPR−NADP complex. This is illustrated in Figure 4, where the sulfate in the structure of *pa*-FPR (Figure 4D) exhibits interactions nearly identical to those shown by the

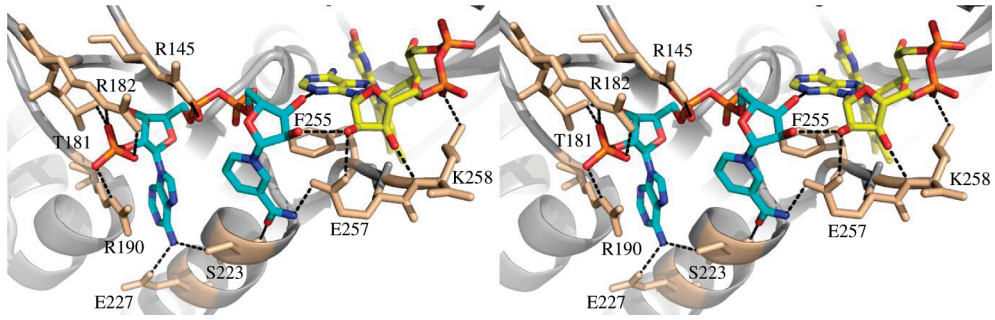

FIGURE 3: Stereoview of a portion of the structure of the *pa*-FPR−NADP complex highlighting the network of stabilizing interactions between the C′-terminal extension (AFVEK^{258}) and the cofactors. FAD is colored yellow and NADP$^+$ cyan, with their N, O, and P atoms colored blue, red, and orange, respectively.

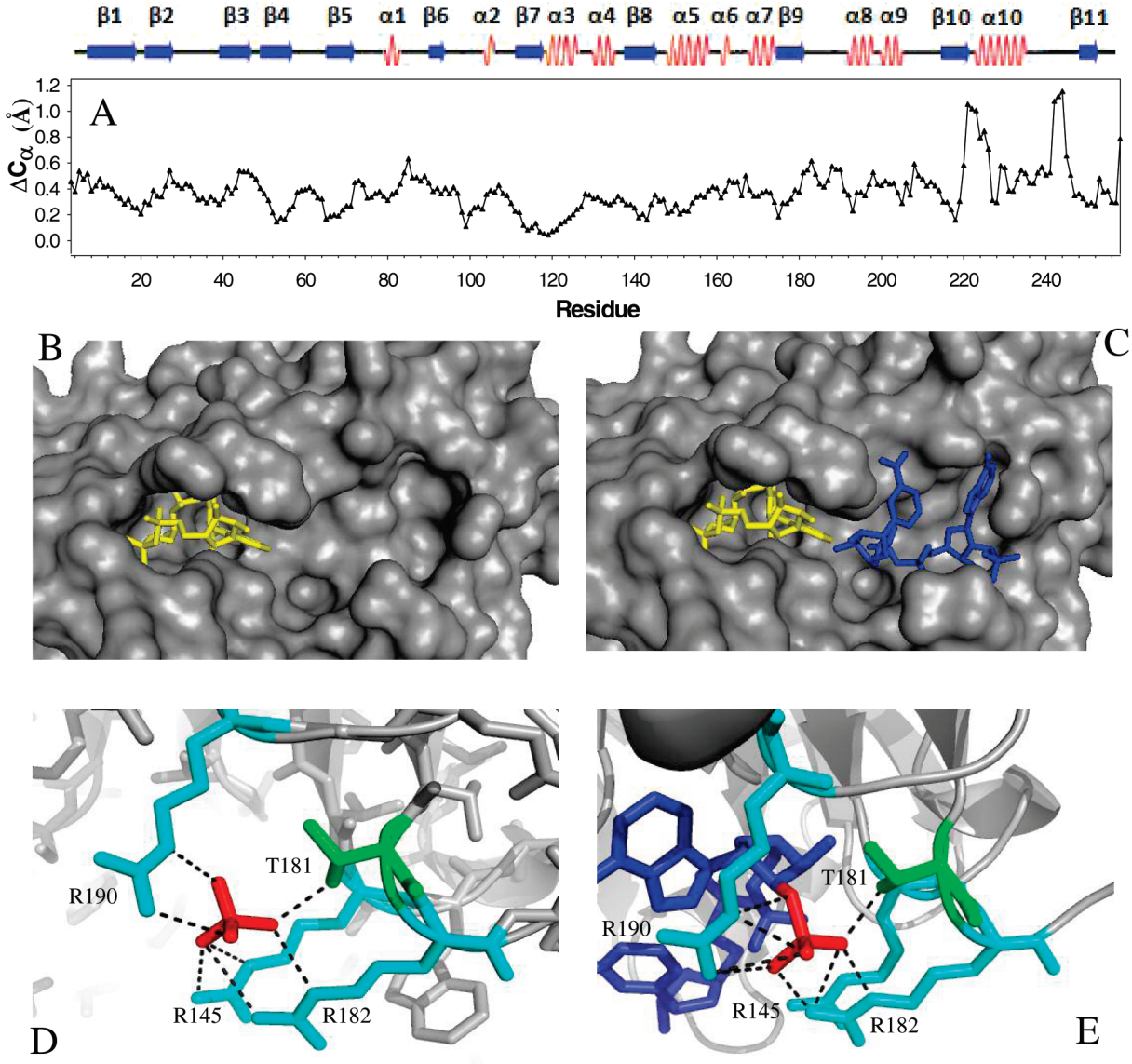

FIGURE 4: (A) Per-residue plot of the difference in the position of α carbons (ΔC_α) obtained upon aligning the structures of *pa*-FPR and that of its NADP$^+$ complex. The average rmsd is 0.47 Å. (B) Close-up view of the empty "NADP-binding pocket" on the surface of *pa*-FPR. The FAD is rendered as yellow sticks. (C) Equivalent view, obtained from the structure of the *pa*-FPR−NADP complex, highlighting NADP$^+$ (blue sticks) lodged in its binding pocket. (D) The structure of *pa*-FPR displays a sulfate ion (red) from the crystallization buffer that occupies the position of the 2′-phosphate group in the *pa*-FPR−NADP complex (E). Note that the interactions exhibited by the phosphate and sulfate ions are nearly identical.

2′-P group in the structure of the *pa*-FPR−NADP complex (Figure 4E). These observations are in good agreement with the idea that the structure of *pa*-FPR harbors a preformed binding pocket, where residues involved in important contacts with the 2′-P group of NADP$^+$ require little or no rearrangement to accommodate the cofactor. Among these residues, R182 and R190 are conserved in bacterial subclass II reductases, Thr181 is conserved in bacterial subclass I

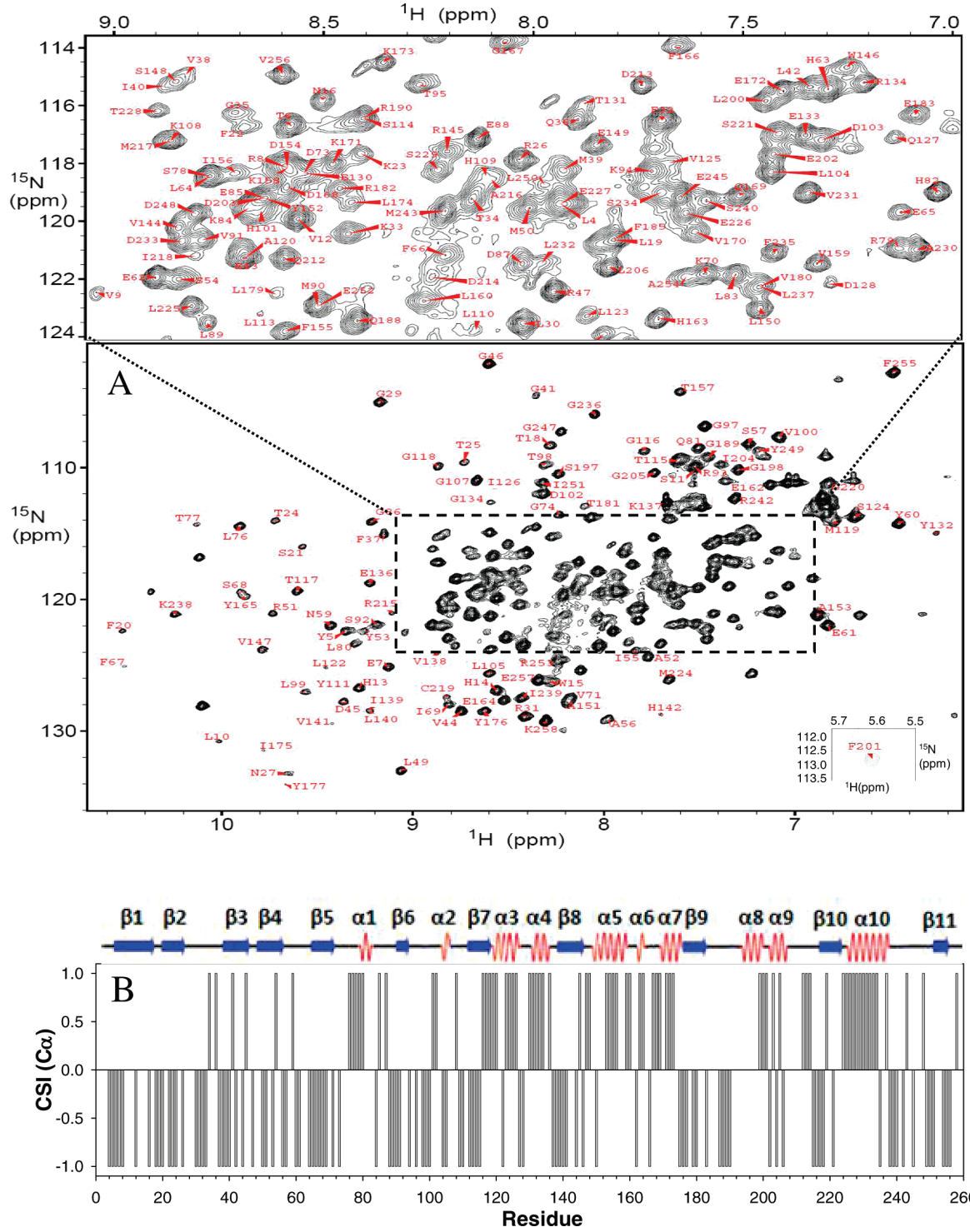

FIGURE 5: (A) ^{1}H−^{15}N HSQC spectrum of 1.5 mM [U-^{13}C,^{15}N]-*pa*-FPR in 50 mM sodium phosphate (pH 7.0) and 6% D_2O, obtained at 25 °C using a Bruker Avance 800 NMR spectrometer. Complex points, 256 (^{1}H) × 2048 (^{15}N); spectral width, 14.4 kHz (^{1}H) and 3.3 kHz (^{15}N); four scans per increment; recycle delay, 0.8 s. (B) Secondary structure in *pa*-FPR inferred from chemical shift indexing (C_α), which can be compared to secondary structure inferred from the X-ray crystal structure (top).

enzymes and substituted for Ser in plant reductases (Ser223 in spinach FNR), and R182 is conserved in all enzymes with known sequence.

Assignment of Amide Backbone Resonances from pa-FPR. NMR spectroscopy studies were carried out to obtain complementary information in solution regarding the binding of $NADP^+$ to *pa*-FPR. Before these investigations could begin, however, it was necessary to obtain sequential backbone resonance assignments. The relatively large molecular mass of the enzyme (29518 Da) posed some challenges. These were overcome with the strategy described below. The ^{1}H−^{15}N HSQC spectrum of *pa*-FPR acquired at 25 °C from a 1.2 mM solution of *pa*-FPR in 50 mM sodium phosphate buffer (pH 7.0) is shown in Figure 5A. These conditions were chosen for the NMR spectroscopic studies because they completely eliminate the slow precipitation of the enzyme when its concentration exceeds 1.5 mM or when the samples are exposed to temperatures above 25 °C for

≥24 h. The spectrum exhibits relatively well dispersed cross-peaks, despite the relatively large molecular mass of the enzyme. Conventional heteronuclear 2D and 3D NMR experiments (see Experimental Procedures) carried out with a sample of *pa*-FPR uniformly labeled with ^{13}C and ^{15}N did not yield enough information to permit full sequential assignments. This is mostly because many residues exhibited weak or absent β carbon (C_β) correlations in TROSY-HNCACB and TROSY-CBCA(CO)NH experiments, which is attributed to efficient transverse relaxation brought about by the dipolar interactions between carbons and their attached protons (*27*). This problem was circumvented by preparing a sample of [U-^{2}H,^{13}C,^{15}N]-*pa*-FPR, which was used to conduct TROSY-HNCACB and TROSY-CBCA(CO)NH experiments for subsequent use with the data obtained from the suite of experiments obtained with [U-^{13}C,^{15}N]-*pa*-FPR. This approach allowed us to assign approximately 85% of the non-proline residues in the enzyme. With respect to [U-^{2}H,^{13}C,^{15}N]-*pa*-FPR, it should be noted that although most of the exchangeable deuterons exchanged for protons during its purification, several residues are clearly protected from exchange because a number of cross-peaks displayed low intensity or were absent when the HSQC spectrum of [U-^{2}H, ^{13}C, ^{15}N]-*pa*-FPR was compared with that obtained from a sample of [U-^{15}N,^{13}C]-*pa*-FPR. Deuterons protected from exchange under native conditions were exchanged by dissolving the triply labeled sample in a urea-containing solution, followed by dialysis in the presence of FAD. This unfolding−refolding procedure resulted in complete replacement of exchangeable deuterons for protons, as indicated by the fact that the TROSY-HSQC spectrum of the resultant enzyme is identical that obtained with doubly labeled *pa*-FPR.

Additional assignments were obtained by incorporating amino acid-selective ^{15}N labeling into *pa*-FPR. This strategy has been successfully utilized in our laboratories to complete the sequential backbone resonance assignments of a paramagnetic, highly helical heme oxygenase from *P. aeruginosa* (*28*). In the context of assigning the backbone resonances from *pa*-FPR, selective labeling was important in our strategy for two main reasons. (1) Nearly undetectable isotopic scrambling was observed with [^{15}N]Leu, [^{15}N]Phe, [^{15}N]Val, and [^{15}N]Thr, which can be seen in the corresponding HSQC spectra (Figure S1A−D). Labeling with [^{15}N]Gly scrambles the label to Ser (Figure S1E). This type of scrambling, however, was found to be useful because it aided in the identification of cross-peaks originating from Ser residues. The label in [^{15}N]Tyr also scrambles, albeit less selectively than the label in [^{15}N]Gly. Nevertheless, the information in the HSQC spectrum of [^{15}N]Tyr-labeled *pa*-FPR (Figure S1F) is valuable because most of the cross-peaks originating from [^{15}N]Tyr are significantly stronger than cross-peaks originating from the scrambled label. In contrast, the label in [^{15}N]Glu and [^{15}N]Asp is highly scrambled, which can be seen in the corresponding HSQC spectra of panels G and H of Figure S1, respectively; these spectra were not very useful to the assignment process. Information obtained from selectively labeled samples was subsequently used in conjunction with the backbone connectivities derived from the suite of three-dimensional experiments described above to make the sequential assignments. This approach was essential to assigning stretches in a sequence where spin systems of key residues within a segment could not be identified due to poor detection of C_β resonances. (2) The simplicity of HSQC spectra obtained from most amino acid selective [^{15}N]-*pa*-FPR samples allows identification of cross-peaks that can be easily overlooked in the spectrum of uniformly ^{15}N-labeled samples, because of overlap with other resonances or due to the relatively low intensity. For instance, in the HSQC spectrum of [[^{15}N]Gly]-*pa*-FPR, the cross-peak in red corresponds to G205 (Figure S2). The same cross-peak is located in a crowded section of the spectrum obtained with the uniformly ^{15}N-labeled enzyme, and thus, it had been overlooked. Its definitive identification in the spectrum of [[^{15}N]Gly]-*pa*-FPR allowed its subsequent sequential assignment with the aid of the suite of three-dimensional experiments described above. In the end, the combined strategies allowed us to make 95% of the backbone assignments in *pa*-FPR, not counting Pro; these assignments are summarized in Table S1.

Once assigned, the backbone chemical shifts were used to identify elements of secondary structure in solution by chemical shift indexing (CSI) (*29*). Results obtained from this process carried out with C_α chemical shifts have been plotted per residue in Figure 5B, where they are compared with elements of secondary structure obtained from the crystal structure of *pa*-FPR using DSSP (http://swift.cmbi.ru.nl/gv/dssp/). It is apparent that secondary structure identified with the aid of NMR spectroscopic studies in solution is consistent with secondary structure obtained from the enzyme in crystal form. The most significant differences are in residues 191−197 (α8) and residues 199−204 (α9). The backbone resonances of residues in α8 were not assigned, most likely because the NH cross-peaks of these residues are very weak or unobservable in HSQC spectra, due to line broadening brought about by segmental dynamic behavior. Cross-peaks from residues 199−204, although observable, are significantly less intense than average cross-peaks, suggesting that these residues are also affected by dynamic conformational exchange. Hence, it is likely that this segment of the structure in solution is conformationally averaged between helical and disordered states; the fact that α8 and α9 are flanked by loops likely facilitates this segmental dynamic behavior. Interestingly, the crystal structure of the *pa*-FPR−NADP complex shows that α8 and α9 are in the proximity of the $NADP^+$ binding site, which suggests the possibility that local conformational plasticity prepares the enzyme to bind the NADP(H) cofactor.

Probing the Binding of $NADP^+$ to pa-FPR in Solution by NMR Chemical Shift Perturbations. The binding of $NADP^+$ to *pa*-FPR was studied by titrating $NADP^+$ into a solution containing ^{15}N-labeled *pa*-FPR, while monitoring induced chemical shift perturbations of amide ^{1}H and ^{15}N resonances with the aid of $^{1}H-^{15}N$ HSQC spectra. The titration induced chemical shift perturbations more than 2 times the average of the weighted chemical shift perturbation (0.12 ppm) in 22 cross-peaks, a characteristic that identifies the corresponding residues as potential sites of interaction with $NADP^+$. The $NADP^+$-dependent gradual shift of cross-peaks indicates that interconversion between $NADP^+$-bound and free forms of the enzyme is fast relative to the NMR time scale (i.e., fast exchange). The titration also caused the disappearance of 18 cross-peaks, which is likely a consequence of exchange between bound and free forms at rates approximately equal

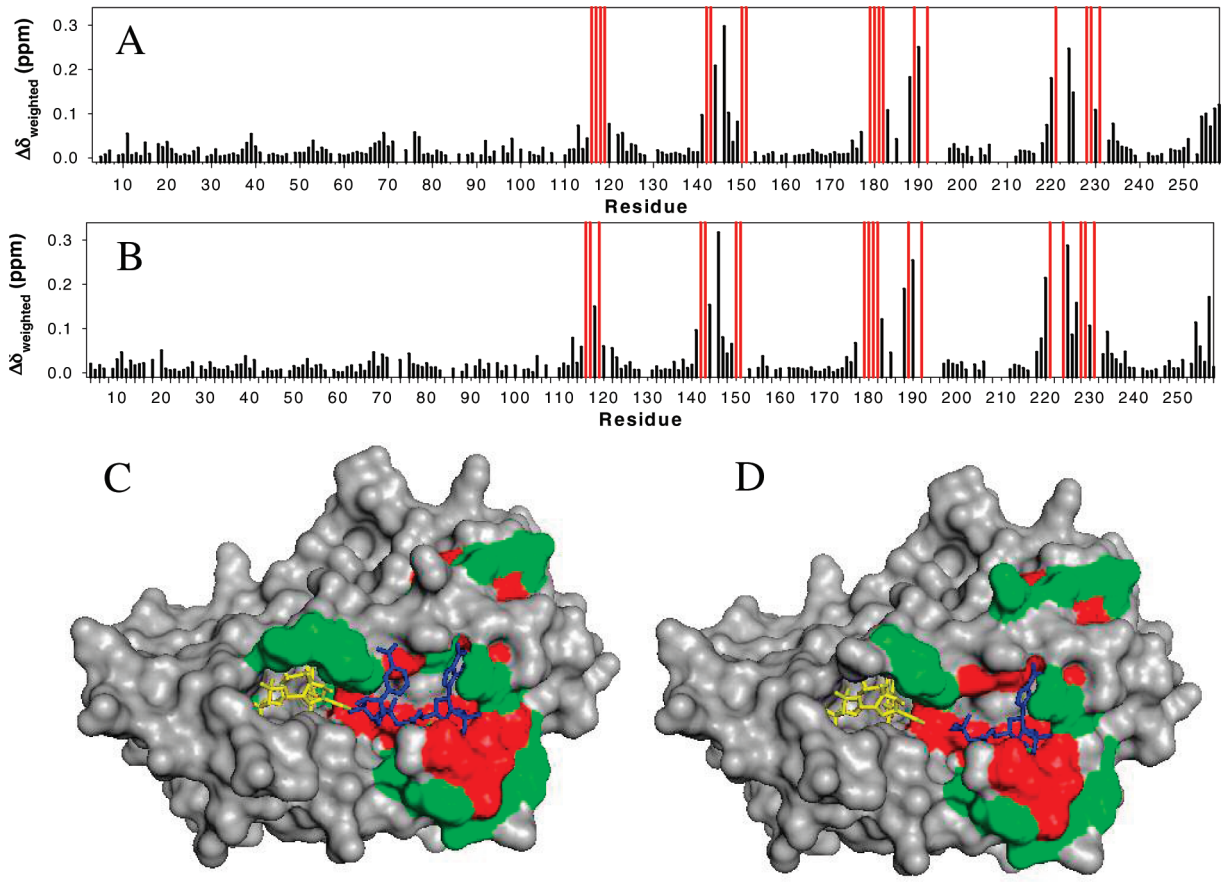

FIGURE 6: (A) Per-residue plot of weighted chemical shift perturbations (black lines) obtained upon titration of a solution of *pa*-FPR with a solution of $NADP^+$ (A) and a solution of ADP (B). The weighted values of chemical shift perturbations were obtained from the relationship $\Delta\delta_{weighted} = \sqrt{[(\Delta\delta N/5)^2 + \Delta\delta H^2]/2}$. The red lines in the plot correspond to residues whose corresponding cross-peaks decrease in intensity and disappeared during the titration. (C) Residues whose corresponding cross-peaks exhibited gradual chemical shift perturbations during the titration with $NADP^+$ are highlighted in green on the surface of the *pa*-FPR−NADP complex, whereas those residues whose cross-peaks decreased in intensity and disappeared during the titration are highlighted in red. FAD and $NADP^+$ are rendered as yellow and blue sticks, respectively. (D) Residues whose cross-peaks were affected during the titration of *pa*-FPR with ADP have been highlighted as in panel C.

to the chemical shift time scale (i.e., intermediate exchange). Cross-peaks exhibiting gradual chemical shift perturbations have been plotted per residue (black in Figure 6A), together with cross-peaks that disappear upon addition of $NADP^+$ (red in Figure 6A). The plot makes it evident that those residues whose chemical shifts exhibit gradual chemical shift perturbations (fast exchange) are clustered with residues whose chemical shifts disappear during the titration, which strongly suggests that line broadening of the latter is a consequence of binding interactions that trigger dynamic events taking place in the intermediate exchange regime. The $NADP^+$-dependent chemical shift perturbation of cross-peaks in fast exchange has been plotted for several representative amino acids (V144, W146, and V147) in Figure S3A and the curve fitted to a model where one molecule of *pa*-FPR binds one molecule of $NADP^+$. This analysis reveals an average dissociation constant (K_d) of 24 μM, a value similar that reported for the binding of $NADP^+$ to spinach FNR (14 μM) at a lower ionic strength (*30*).

Residues whose N−H cross-peaks exhibit weighted chemical shift perturbations larger than 0.08 ppm upon titration of *pa*-FPR with $NADP^+$ are highlighted in green on the X-ray crystal structure of the *pa*-FPR−NADP complex (Figure 6C), whereas residues whose N−H cross-peaks disappear are highlighted in red. It is reassuring that the chemical shifts of amide cross-peaks corresponding to residues identified in the crystal structure as being in the proximity of $NADP^+$ are perturbed by the presence of $NADP^+$. Among these, cross-peaks from residues interacting with the 2′-P group of $NADP^+$, Thr181, Arg182, and Arg190 (see Figure 3), are broadened and disappear due to exchange in the intermediate regime, whereas the cross-peak originating from Glu257, which interacts with the amide NH_2 group of the nicotinamide ring, exhibits perturbations in the fast exchange regime. Cross-peaks for Arg145 and Ser223, which interact with pyrophosphate group P1, and with both the nicotinamide amide and the 2′-P groups of $NADP^+$, respectively, have not been assigned. A comparison of the X-ray crystal structures of *pa*-FPR and the *pa*-FPR−NADP complex has been made in panels B and C of Figure 4, which shows that the structure of *pa*-FPR has a preformed $NADP^+$-binding pocket where the cofactor binds with minimal perturbations of the structure of the enzyme. In Figure 6C, the cofactors have been rendered in sticks to illustrate the fact that residues comprising the "internal walls" of the $NADP^+$-binding pocket are highlighted in red and green. This observation indicates that the surface of interaction in the structure of $NADP^+$ includes the internal walls of the $NADP^+$-binding pocket and demonstrates that the chemical shift perturbations and line broadening effects brought about by the binding of $NADP^+$ in solution delineate a binding surface highly consistent with that observed in the crystal structure. Hence,

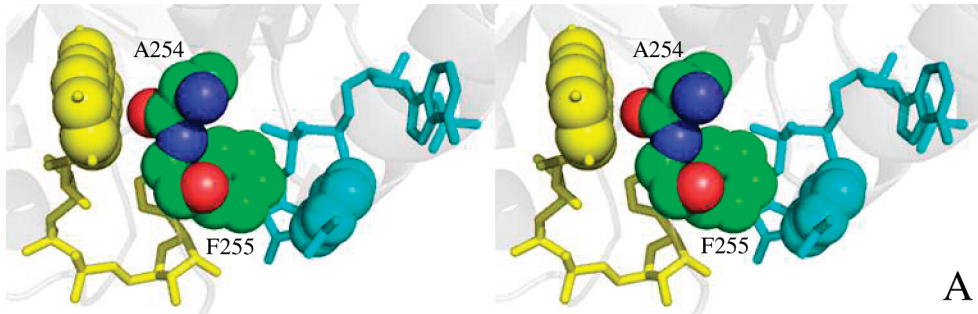

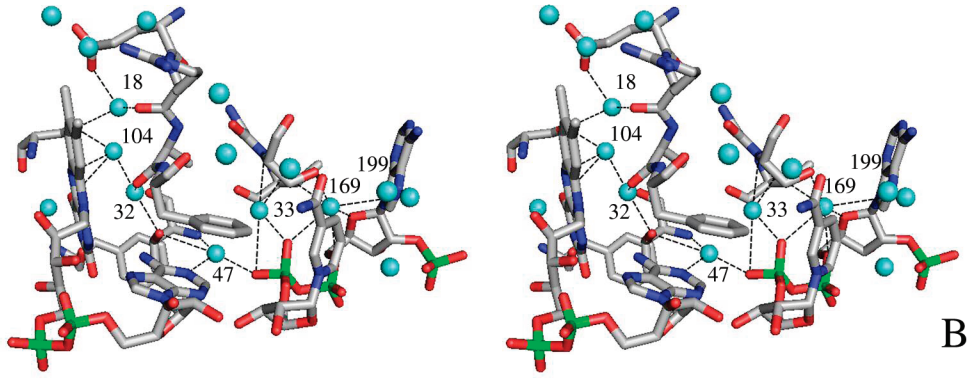

S. oleracea	297	IEYKRQLKKAEQWNVEVY------	314
P. aeruginosa	237	LKISPRMGEPGDYLIERAFVEK--	258
A. vinelandii	237	LKISPRMGEPGDYLIERAFVEK--	258
P. putida	238	LKISPRMREPGDYLIERAFVEK--	259
P. syringae	238	LTVSPRMREPGDYLIERAFVEK--	259
Azoarcus sp.	237	FKISRHIGEPGDYVIERAFVEK--	258
B. parapertussis	237	FEVSPGVGEPGDYVFERAFVDK--	258
X. fastidiosa	238	FNASARIGSPGDYVFERAFVDQ--	259
N. meningitidis	237	LTVSPKTGVRGDYLIERAFVDQ--	258
R. rubrum	237	FREG-NTGEPGHFVIEKAFVEK--	257
B. japonicum	237	FVEG-NHSQPGHFVIEKAFVER--	257
C. crescentus	246	LKEG-SNAEPGDFVIERAFVG---	265
R. capsulatus	250	LREG-ANSEPREFVVEKAFVGEGI	272
R. sphaeroides	246	LREG-ANSEPLQYVVEKAFVGDGI	268
S. meliloti	251	LTEG-ANNKPAEFVIERAFVG---	270

C

FIGURE 7: (A) Stereoview of a possible electron tunneling path which starts with the T-stacking of the nicotinamide ring (cyan) and Phe255 aromatic side chain and continues across the peptide bond into Ala255 and across its carbonyl oxygen into the isoalloxazine ring of FAD (yellow). (B) Stereoview showing that in the context of sequential electron−proton−electron transfer, several structural waters network the nicotinamide and isoalloxazine reactive sites, suggesting a possible path for proton translocation. (C) Amino acid sequence alignment of bacterial subclass I FPR enzymes showing that residues A254, F255, and V256 from the AFVxx motif in the C′-terminal extension are conserved. The C′-terminal sequence of spinach FNR, highlighting the terminal Tyr of plastidic FNRs, is shown for comparison.

observations made with the enzyme in solution also indicate that the structure of *pa*-FPR harbors a preformed $NADP^+$-binding pocket.

Current models of NADP(H) binding to plastidic FNRs propose that parallel stacking of the nicotinamide ring onto the isoalloxazine ring to form a productive complex for direct hydride transfer requires displacement of the side chain from the terminal Tyr. Equilibrium binding studies conducted with spinach FNR revealed that its binding affinity for $NADP^+$ is approximately 7 times lower than its affinity for adenonsine 2′,5′-diphosphate (ADP) (*30*), which lacks the nicotinamide nucleotide moiety. These observations have been interpreted in the context of the binding model to support the idea that NADP(H) binding to plastidic FNRs is a two-step process, with the first step involving strong interactions between the 2′-adenosyl phosphate and FNR and the second step requiring displacement of the terminal Tyr to allow the nicotinamide ring to stack parallel to the isoalloxazine ring of FAD. In

this model, the second step, which is thought to be energetically costly, has been invoked to explain the higher affinity of FNR for ADP relative to $NADP^+$ (*17, 31*). It was therefore of interest to examine the binding of ADP to *pa*-FPR and compare the results with those described above for the binding of $NADP^+$. Hence, ADP was titrated into a solution containing ^{15}N-labeled *pa*-FPR while monitoring induced chemical shift perturbations in $^1H-^{15}N$ HSQC spectra. Remarkably, titration with ADP revealed a pattern of perturbed residues (Figure 6B) nearly identical to the pattern obtained upon binding of $NADP^+$ to *pa*-FPR (Figure 6A). This fact is also evident in the corresponding color-coded representation obtained by mapping residues whose cross-peaks exhibit chemical shift perturbations (green) and line broadening effects (red) on the structure of the *pa*-FPR−NADP complex (Figure 6D). Chemical shift perturbations induced by addition of ADP to *pa*-FPR for several representative amino acids (V144, W146, and V147) have been plotted and fitted to a model with a 1:1 stoichiometry (Figure S3B). This process reveals an average K_d of 32 μM, a value that is slightly larger than that measured for the *pa*-FPR−NADP complex (see above). The similarity in the magnitudes of K_d values obtained for the binding of $NADP^+$ and the competitive inhibitor ADP indicates that stabilization of the *pa*-FPR−NADP complex is derived mainly from interactions between the polypeptide and the adenosine 2′,5′-diphosphate moiety in $NADP^+$. In contrast to observations made with spinach FNR, however, the binding affinity of *pa*-FPR for $NADP^+$ is slightly greater than its affinity for ADP, which indicates that the nicotinamide nucleotide moiety does not undergo destabilizing interactions with the enzyme, which is thought to be the case in the binding of $NADP^+$ to plastidic FNRs. It is therefore likely that $NADP^+$ binding to *pa*-FPR occurs in one step, rather than two, which is thought to be the case when it binds to FNRs.

The C′-Terminal Sequence Is Unlikely To Experience High Degree of Conformational Disorder. As pointed out above, the X-ray crystal structure of *pa*-FPR revealed a network of interactions involving the C′-terminal extension and the two cofactors, strongly suggesting that the C′-terminal sequence of *pa*-FPR is not likely to be displaced readily to allow parallel stacking of the nicotinamide and isoalloxazine rings. To examine whether the C′-terminal tail is undergoing conformational fluctuations in solution, we looked for signs of dynamic motions manifested in the characteristics of HSQC cross-peaks. Peaks significantly affected by slow conformational exchange (microseconds to milliseconds) typically show decreased intensity and/or larger line widths than those originating from regions of a protein unaffected by such motions, provided the interconverting species in equilibrium are sufficiently populated (*32, 33*). In this analysis, we expected that residues located near the nicotinamide and isoalloxazine rings would be most significantly affected by conformational exchange and consequently display enhanced line widths and/or decreased intensity relative to the average for all other peaks in the spectrum. This notion was probed in solution by acquiring $^1H-^{15}N$ HSQC spectra of *pa*-FPR, the *pa*-FPR−NADP complex, and the *pa*-FPR−ADP complex at different temperatures (35, 25, and 15 °C) and at a ^1H frequency of 600 MHz. Cross-peaks corresponding to the $AFVEK^{258}$ sequence exhibit ^1H line widths and cross-peak intensities that are very similar to the average ^1H line widths and average cross-peak intensity at each of the temperatures in all spectra, implying that alternative conformations are not significantly populated in the range of temperature explored, thus suggesting that the C′-terminal extension is unlikely to undergo significant conformational changes in the presence or absence of $NADP^+$. It is important to note that the data at hand cannot completely rule out the presence of a dynamic equilibrium between a very small population of molecules, where the cofactors attain a productive conformation, and a bulk population, where the conformation of FAD and $NADP^+$ is very similar to that in the crystal structure, which dominates the HSQC spectrum. If this small population is indeed present, it may be possible to study it with the aid of detailed dynamic studies, including analysis or R_2 relaxation dispersion data (*32, 34*). It is important to consider, however, that the population with a productive conformation is small in the plastidic FNRs (~10%) (*17*), where only the side chain of the terminal Tyr has to move to allow the nicotinamide ring of $NADP^+$ to enter the FAD-isoalloxazine environment. In comparison, the structure of the *pa*-FPR−NADP complex indicates that for the nicotinamide ring to enter the isoalloxazine environment, a much larger conformational rearrangement is necessary, which involves the $AFVEK^{258}$ terminal extension. Moreover, it is also important to consider that the conformation of FAD in *pa*-FPR is bent and therefore distinct from the extended FAD conformation in plastidic FNRs (see Figure 1). The bent conformation of FAD in bacterial FPR enzymes places the adenine ring between the isoalloxazine and nicotinamide rings (see Figure 3). Consequently, for the nicotinamide ring to enter the isoalloxazine ring environment in bacterial FPRs, the FAD has to undergo a large conformational change, which very likely would expose a large portion of the cofactor to the aqueous environment, thus making it prone to be released from the enzyme. It is also conceivable that binding of NADPH instead of $NADP^+$ promotes the large conformational changes that would be needed to form a productive complex in FPRs. This scenario, however, is also unlikely because the conformational changes necessary would still involve the large amplitude motions of the C′-terminal sequence and of the FAD cofactor discussed above. Hence, together, these considerations strongly suggest that the large conformational changes that would have to take place on FPR to allow parallel and adjacent placement of the nicotinamide and isoalloxazine rings for direct hydride transfer are unlikely. Nevertheless, additional experimentation is necessary to continue to probe these ideas.

Potential Implications for the Mechanism of NADPH Oxidation by FPRs. The observations described above suggest that conformational reorganization of the C′-terminal peptide and of the $NADP^+$ and FAD cofactors to allow formation of a productive complex for direct hydride transfer is unlikely to take place in the *pa*-FPR−NADP complex. In this context, it is important to consider that extensive fundamental investigations of the mechanism of NAD(P)H oxidation have demonstrated that hydride transfer can also occur in a stepwise manner by sequential electron−proton−electron transfer (*35–44*) (eq 1).

$$\mathrm{NAD(P)H} + \mathrm{A} \rightarrow \mathrm{NAD(P)H^{\bullet+} \cdots A^{\bullet}} \rightarrow \mathrm{NAD(P)^{\bullet} \cdots AH^{\bullet+}} \rightarrow \mathrm{NAD(P)^{+}} + \mathrm{HA} \quad (1)$$

These investigations documented the formation of radical cations and radicals of NAD(P)H and its analogues, which have been characterized with the aid of electronic absorption

and EPR spectroscopic methods. The formation and detection of these reactive species indicated that the oxidation of NAD(P)H and its analogues can occur stepwise via electron−proton−electron transfer of hydride, if the acceptor is also capable of undergoing a stepwise two-electron reduction. This point has been recently underscored with the EPR and electronic absorption spectroscopic detection of a radical cation of an NADH analogue in the thermal two-electron reduction of a quinone (*35*). Moreover, it has also been demonstrated that in the absence of H_2O_2, the oxidation of NADH by native horseradish peroxidase (HRP) begins with a single electron transfer from NADH to ferric HRP to form the $NADH^{\bullet+}$ radical cation and ferrous peroxidase (*39*). A similar stepwise oxidation of NADPH is thought to be operative in the rescue of inactive catalase (*45*). Hence, under appropriate circumstances, the oxidation of NAD(P)H by sequential electron−proton−electron transfer of hydride is a viable alternative mechanistic path to the well-known direct mechanism involving synchronous transfer of a proton and two electrons.

It has also been established that long-range (up to 30 Å) electron transfer through proteins occurs via tunneling pathways, which involve dominant bonding and nonbonding interactions coupling donor and acceptor. Coupling through covalent and hydrogen bonds is stronger than coupling through van der Waals gaps (*46–48*), and these differences in the details of specific paths involved in distinct systems account for the dependence of electron transfer rates on the particular aspects of the protein structure that mediate coupling of donor and acceptor (*48*). In this frame, it is interesting that the structure of the *pa*-FPR−NADP complex places C4 of the nicotinamide ring 14.5 Å from N5 of the isoalloxazine ring. Further inspection of the structure suggests a "tunneling pathway" connecting the nicotinamide ring in NADP(H) with the isoalloxazine ring in FAD. This putative path (Figure 7A) can be thought to start with the T-stacking of the nicotinamide and Phe255 rings, continue along Phe255 into Ala254 across the peptide bond, and finally communicate with the isoalloxazine ring via the Ala254 carbonyl oxygen, which is 2.93 Å from N10 and 3.93 Å from N5 in the isoalloxazine ring. In this putative mechanism, electron tunneling from the nicotinamide to the isoalloxazine ring would form an $NADPH^{\bullet+}$ radical cation analogous that shown in eq 1. Radical cations of NADH model compounds are known to be significantly more acidic than their neutral precursors (*42*); thus, the $NADPH^{\bullet+}$ radical cation formed upon tunneling of one electron would be expected to lose a proton, thereby forming an $NADP^{\bullet}$ radical, as shown in eq 1. Tunneling of a second electron from the latter would form the closed shell $NADP^+$. Accordingly, the electron acceptor, FAD, can be reduced in two sequential one-electron and one-proton transfer reactions (*49, 50*). In the context of a stepwise, electron−proton−electron, hydride transfer, it is also interesting to note a network of structural water molecules in the structure of the *pa*-FPR−NADP complex, which may facilitate translocation of a proton from NADPH to FAD (Figure 7B). In the same frame, it is also interesting to consider that amino acid alignment of bacterial subclass I FPR enzymes (Figure 7C) shows that the $AFVEK^{258}$ extension of *pa*-FPR is present in all bacterial subclass I FPR enzymes of known sequence (AFVxx). Furthermore, it is noteworthy that residues A254 and F255 in this motif, which we implicate in the putative path of electron transfer (Figure 7A), are conserved.

It is important to emphasize that one-electron reduction of $NAD(P)^+$ analogues does not result in an overall hydride ion addition in the same manner in which one-electron oxidation of NAD(P)H triggers a multistep hydride ion release (*38*). Hence, the proposed mechanism of NADPH oxidation by FPRs is consistent with the fact that these enzymes function by exclusively oxidizing the cofactor, unlike their plastidic counterparts, which function in the "normal" sense by reducing $NADP^+$ via hydride transfer from $FADH_2$ or in the "inverse" sense by oxidizing NADPH. It is therefore possible that the need to reduce $NADP^+$ has placed evolutionary pressure on the structure of plastidic FNRs to allow parallel placement of the nicotinamide and isoalloxazine rings for efficient hydride transfer and reduction of $NADP^+$ to support the high level of electron flow needed in the photosynthetic process of CO_2 fixation (*5*). In comparison, the function of FPR enzymes, which is solely the oxidation of NADPH, was acquired with minor modifications of the C′-terminal domain, which make the direct transfer of hydride ($NADP^+$ reduction) unlikely but a multistep hydride transfer (NADPH oxidation) operative. These ideas, which stem from the X-ray crystallographic and NMR spectroscopic observations of the *pa*-FPR−NADP complex, have to be tested experimentally. Their discussion in this report is aimed at providing a frame of ideas consistent with experimental observations and to stimulate future experimentation directed at elucidating the mechanism of NADPH oxidation by FPR enzymes.

SUPPORTING INFORMATION AVAILABLE

$^1H-^{15}N$ HSQC spectra of [^{15}N]Leu, [^{15}N]Phe, [^{15}N]Thr, [^{15}N]Val, [^{15}N]Gly, [^{15}N]Tyr, [^{15}N]Glu, and [^{15}N]Asp, $^1H-^{15}N$ HSQC spectrum of [[^{15}N]Gly]-*pa*-FPR compared to the HSQC spectrum of [U-^{15}N]-*pa*-FPR, plots for the titration of [U-^{15}N]-*pa*-FPRP with $NADP^+$ and with ADP, and a table of backbone resonance assignments for *pa*-FPR. This material is available free of charge via the Internet at http://pubs.acs.org.

REFERENCES

1. Arakaki, A. K., Ceccarelli, E. A., and Carrillo, N. (1997) Plant-Type Ferredoxin $NADP^+$ Reductases: A Basal Structural Framework and a Multiplicity of Functions. *FASEB J. 11*, 133–140.
2. Shin, M., and Arnon, D. I. (1965) Enzymic Mechanisms of Pyridine Nucleotide Reduction in Chloroplasts. *J. Biol. Chem. 240*, 1405–1411.
3. Liochev, S. I., Hausladen, A., Beyer, W. F. J., and Fridovich, I. (1994) NADPH:Ferredoxin Oxidoreductase Acts as a Paraquat Diaphorase and is a Member of the *soxRS* Regulon. *Proc. Natl. Acad. Sci. U.S.A. 91*, 1328–1331.
4. Yannone, S. M., and Burgess, B. K. (1998) The Seven-Iron Fdl from *Azotobacter vinelandii* Regulates the Expression of NADPH: Ferredoxin Reductase vian an Oxidative Stress Response. *J. Biol. Inorg. Chem. 3*, 253–258.
5. Bittel, C., Tabares, L. C., Armesto, M., Carrillo, N., and Cortez, N. (2003) The Oxidant-Responsive Diaphorase of *Rhodobacter capsulatus* is a Ferredoxin (flavodoxin)-NADP(H) Reductase. *FEBS Lett. 553*, 408–412.
6. Wang, A., Zeng, Y., Han, H., Weeratunga, S., Morgan, B. N., Moënne-Loccoz, P., Schönbrunn, E., and Rivera, M. (2007) Biochemical and Structural Characterization of *Pseudomonas aeruginosa* Bfd and FPR: Ferredoxin $NADP^+$ Reductase and

Not Ferredoxin is the Redox Partner of Heme Oxygenase under Iron-Starvation Conditions. *Biochemistry 46*, 12198–12211.
7. Prasad, G. S., Kresge, N., Muhlberg, A. B., Shaw, A., Jung, Y. S., Burgess, B. K., and Stout, C. D. (1998) The Crystal Structure of NADPH:Ferredoxin Reductase from *Azotobacter vinelandii*. *Protein Sci. 7*, 2541–2549.
8. Nogués, I., Pérez-Dorado, I., Frago, S., Bittel, C., Mayhew, S. G., Gómez-Moreno, C., Hermoso, J. A., Medina, M., Cortez, N., and Carrillo, N. (2005) The Ferredoxin-NADP(H) Reductase from *Rhodobacter capsulatus*: Molecular Structure and Catalytic Mechanism. *Biochemistry 44*, 11730–11740.
9. Ingelman, M., Bianchi, V., and Eklund, H. (1997) The Three-Dimensional Structure of Flavodoxin Reductase from *Escherichia coli* at 1.7 Å Resolution. *J. Mol. Biol. 268*, 147–157.
10. Ceccarelli, E. A., Arakaki, A. K., Cortez, N., and Carrilo, N. (2004) Functional Plasticity and Catalytic Efficiency in Plant and Bacterial Ferredoxin-(NADP(H) Reductases. *Biochim. Biophys. Acta 1698*, 155–165.
11. Karplus, P. A., Daniels, M. J., and Herriott, D. J. R. (1991) Atomic Structure of Ferredoxin-NADP$^+$ Reductase: Prototype for a Structurally Novel Flavoenzyme Family. *Science 251*, 60–66.
12. Bruns, C. M., and Karplus, P. A. (1995) Refined Crystal Structure of Spinach Ferredoxin Reductase at 1.7 Å Resolution: Oxidized Reduced and 2′-phospho-5′AMP Bound States. *J. Mol. Biol. 247*, 125–145.
13. Hermoso, J. A., Mayoral, T., Faro, M., Gómez-Moreno, C., Sanz-Aparicio, J., and Medina, M. (2002) Mechanism of Coenzyme Recognition and Binding Revealed by Crystal Structure Analysis of Ferredoxin-NADP$^+$ Reductase Complexed with NADP$^+$. *J. Mol. Biol. 319*, 1133–1142.
14. Serre, L., Vellieux, F. M. D., Medina, M., Gómez-Moreno, C., Fontecilla-Camps, J. C., and Frey, M. (1996) X-ray Structure of the Ferredoxin:NADP$^+$ Reductase from the Cyanobacterium *Anabaena* PCC7119 at 1.8 Å Resolution, and Crystallographic studies of NADP$^+$ Binding at 2.25 Å Resolution. *J. Mol. Biol. 263*, 20–39.
15. Pai, E. F., Karplus, P. A., and Schulz, G. E. (1988) Crystallographic Analysis of the Binding of NADPH, NADPH Fragments, and NADPH Analogues to Glutathione Reductase. *Biochemistry 27*, 4465–4474.
16. Karplus, P. A., and Schulz, G. E. (1989) Substrate Binding and Catalysis by Glutathione Reductase as Derived from Refined Enzyme: Substrate Crystal Structures at 2 Å Resolution. *J. Mol. Biol. 210*, 163–180.
17. Deng, Z., Aliverti, A., Zanetti, G., Arakaki, A. K., Ottado, J., Orellano, E. G., Calcaterra, N. B., Ceccarelli, E. A., Carrillo, N., and Karplus, P. A. (1999) A Productive NADP$^+$ Binding Mode of Ferredoxin-NADP$^+$ Reductase Revealed by Protein Engineering and Crystallographic Studies. *Nat. Struct. Biol. 6*, 847–853.
18. Morgan, W. D., Kragt, A., and Feeney, J. (2000) Expression of deuterium-isotope-labelled protein in the yeast *Pichia pastoris* for NMR studies. *J. Biomol. NMR 17*, 337–347.
19. Cheng, H., Westler, W. M., Xia, B., Oh, B.-H., and Markley, J. L. (1995) Protein expression, selective isotopic labeling, and analysis of hyperfine-shifted NMR signals of *Anabaena* 7120 vegetative [2Fe-2S]ferredoxin. *Arch. Biochem. Biophys. 316*, 619–634.
20. Rodriguez, J. C., Wilks, A., and Rivera, M. (2006) Backbone NMR Assignments and H/D Exchange Studies on the Ferric Azide- and Cyanide-Inhibited Forms of *Pseudomonas aeruginosa* Heme Oxygenase. *Biochemistry 45*, 4578–4592.
21. Wishart, D. S., Bigam, C. G., Yao, J., Abildgaard, F., Dyson, H. J., Oldfield, E., Markley, J. L., and Sykes, B. D. (1995) ^{1}H, ^{13}C and ^{15}N Chemical Shift Referencing in Biomolecular NMR. *J. Biomol. NMR 6*, 135–140.
22. Kabsch, W. (1993) Automatic Processing of Rotation Diffraction Data from Crystals of Initially Unknown Symmetry and Cell Constraints. *J. Appl. Crystallogr. 26*, 795–800.
23. Brunger, A. T., Adams, P. D., Clore, G. M., DeLano, W. L., Gros, P., Grosse-Kunstleve, R. W., Jiang, J. S., Kuszewski, J., Nilges, M., Pannu, N. S., Read, R. J., Rice, L. M., Simonson, T., and Warren, G. L. (1998) Crystallography & NMR System: A New Software Suite for Macromolecular Structure Determination. *Acta Crystallogr. D54*, 905–921.
24. Jones, T. A., and Zhou, J. Y. (1991) Improved Methods for Binding Protein Models in Electron Density Maps and the Location of Errors in These Models. *Acta Crystallogr. A47*, 110–119.
25. Medina, M., Luquita, A., Tejero, J., Hermoso, J., Mayoral, T., Sanz-Aparicio, J., Grever, K., and Gómez-Moreno, C. (2001) Probing the Determinants of Coenzyme Specificity in Ferredoxin NADP$^+$ Reductase by Site-Directed Mutagenesis. *J. Biol. Chem. 276*, 11902–11912.
26. Medina, M., and Gómez-Moreno, C. (2004) Interaction of Ferredoxin-NADP$^+$ Reductase with its Substrates: Optimal Interaction for Efficient Electron Transfer. *Photophys. Res. 79*, 113–131.
27. Permi, P., and Annila, A. (2004) Coherence Transfer in Proteins. *Prog. Nucl. Magn. Reson. Spectrosc. 44*, 97–137.
28. Rodríguez, J. C., Zeng, Y., Wilks, A., and Rivera, M. (2007) The Hydrogen-Bonding Network in Heme Oxygenase Also Functions as a Modulator of Enzyme Dynamics: Chaotic Motions upon Disrupting the H-Bond Network in Heme Oxygenase from *Pseudomonas aeruginosa*. *J. Am. Chem. Soc. 129*, 11730–11742.
29. Wishart, D. S., and Sykes, B. D. (1994) The ^{13}C Chemical-Shift Index: A Simple Method for the Identification of Protein Secondary Structure Using ^{13}C Chemical Shift Data. *J. Biomol. NMR 4*, 171–180.
30. Batie, C. J., and Kamin, H. (1986) Association of Ferredoxin-NADP$^+$ Reductase with NADP(H). Specificity and Oxidation-Reduction Properties. *J. Biol. Chem. 261*, 11214–11223.
31. Carrillo, N., and Ceccarelli, E. A. (2003) Open Questions in Ferredoxin-NADP$^+$ Reductase Catalytic Mechanism. *Eur. J. Biochem. 270*, 1900–1915.
32. Millet, O., Loria, J. P., Kroenke, C. D., Pons, M., and Palmer, A. G. (2000) The Static Magnetic Field Dependence of Chemical Exchange Line Broadening Defines the NMR Chemical Shift Time Scale. *J. Am. Chem. Soc. 122*, 2867–2877.
33. Zhang, O., and Forman-Kay, J. D. (1997) NMR Studies of Unfolded States of an SH3 Domain in Aqueous Solution and Denaturing Conditions. *Biochemistry 36*, 3959–3970.
34. Boehr, D. D., McElheny, D., Dyson, H. J., and Wright, P. E. (2006) The Dynamic Energy Landscape of Dihydrofolate Reductase Catalysis. *Science 313*, 1638–1642.
35. Yuasa, J., Yamada, S., and Fukuzumi, S. (2008) Detection of a Radical Cation of an NADH Analogue in Two-Electron Reduction of a Protonated *p*-Quinone Derivative by an NADH Analogue. *Angew. Chem., Int. Ed. 47*, 1068–1071.
36. Fukuzumi, S., Inada, O., and Suenobu, T. (2002) Direct Detection of Radical Cations of NADH Analogues. *J. Am. Chem. Soc. 124*, 14538–14539.
37. Fukuzumi, S., Inada, O., and Suenobu, T. (2003) Mechanisms of Electron-Transfer Oxidation of NADH Analogues and Chemiluminescence. Detection of the Keto and Enol Radical Cations. *J. Am. Chem. Soc. 125*, 4808–4816.
38. Gębicki, J., Marcinek, A., and Zielonka, J. (2004) Transient Species in the Stepwise Interconversion of NADH and NAD$^+$. *Acc. Chem. Res. 37*, 379–386.
39. Afanasyeva, M. S., Taraban, M. B., Purtov, P. A., Lashina, T. V., and Grissom, C. B. (2006) Magnetic Spin Effects in Enzymatic Reactions: Radical Oxidation of NADH by Horseradish Peroxidase. *J. Am. Chem. Soc. 128*, 8651–8658.
40. Yuasa, J., and Fukuzumi, S. (2006) Mechanistic Borderline Between One-Step Hydrogen Transfer and Sequential Transfers of Electron and Proton in Reactions of NADH Analogues with Triplet Excited States of Tetrazines and Ru(bpy)$^{2+}$. *J. Am. Chem. Soc. 128*, 14281–14292.
41. Fukuzumi, S., Ohkubo, K., Tokuda, Y., and Suenobu, T. (2000) Hydride Transfer from 9-Substituted 10-Methyl-9,10-dihydroacridines to Hydride Acceptors via Charge-Transfer Complexes and Sequential Electron-Proton-Electron Transfer. A negative Temperature Dependence. *J. Am. Chem. Soc. 122*, 4286–4294.
42. Anne, A., Hapiot, P., Moiroux, J., Neta, P., and Savéant, J. M. (1992) Dynamics of Proton Transfer from Cation Radicals. Kinetic and Thermodynamic Acidities of Cation Radicals of NADH Analogues. *J. Am. Chem. Soc. 114*, 4694–4701.
43. Zielonka, J., Marcinek, A., Huben, K., and Gębicki, J. (2003) Direct Observation of NADH Radical Cation Generated in Reactions with One-Electron Oxidants. *J. Phys. Chem. A 107*, 9860–9864.
44. Marcinek, A., Adamus, J., Huben, K., Gębicki, J., Bartczak, T. J., Bednarek, P., and Bally, T. (2000) Hydrogen-Transferred Radical Cations of NADH Model Compounds. 1. Spontaneous Tautomerization. *J. Am. Chem. Soc. 122*, 437–443.
45. Almarsson, O., Sinha, A., Gopinath, E., and Bruice, T. C. (1993) Mechanism of One-Electron Oxidation of NAD(P)H and Function of NADPH Bound to Catalase. *J. Am. Chem. Soc. 115*, 7093–7102.
46. Beratan, D. N., Betts, J. N., and Onuchic, J. N. (1991) Protein Electron Transfer Rates Set by the Bridging Secondary and Tertiary Structure. *Science 252*, 1285–1288.

47. Beratan, D. N., Onuchic, J. N., Betts, J. N., Bowler, B. E., and Gray, H. B. (1990) Electron-Tunneling Pathways in Ruthenated Proteins. *J. Am. Chem. Soc. 112*, 7915–7921.
48. Gray, H. B., and Winkler, J. R. (2005) Long-Range Electron Transfer. *Proc. Natl. Acad. Sci. U.S.A. 102*, 3534–3539.
49. Bhattacharyya, S., Stankovich, M. T., Truhlar, D. G., and Gao, J. (2007) Combined Quantum Mechanical and Molecular Mechanical Simulations of One- and Two-Electron Reduction Potentials of Flavin Cofactor in Water, Medium-Chain Acyl-CoA Dehydrogenase, and Cholesterol Oxidase. *J. Phys. Chem. 111*, 5279–5742.
50. Ghisla, S., and Massey, V. (1989) Mechanisms of Flavoprotein-Catalyzed Reactions. *Eur. J. Biochem. 181*, 1–17.

BI8007356